IEEE Transactions on Power Electronics, 2019. DOI: 10.1109/TPEL.2019.2892397

A Low-Loss Inductor Structure and Design Guidelines for High-Frequency Applications

Rachel S. Yang, *Student Member, IEEE,* Alex J. Hanson, *Student Member, IEEE,*
Bradley A. Reese, *Member, IEEE,* Charles R. Sullivan, *Fellow, IEEE,* and David J. Perreault *Fellow, IEEE*

***Abstract*—Operation in the HF regime (3–30 MHz) has potential for miniaturizing power electronics, but designing small, efficient inductors at HF can be challenging. At these frequencies, losses due to skin and proximity effects are difficult to reduce, and gaps needed to keep B fields low in the core add fringing field loss. We propose a low-loss inductor structure with step-by-step design guidelines for HF applications. The structure achieves low loss through double-sided conduction in its single-layer winding and through quasi-distributed gaps. An example $\sim 15\,\mu$H inductor designed using the proposed design guidelines achieved an experimental quality factor of 720 at 3 MHz and 2 A (peak) of ac current. The inductor also improved a high-current-swing power converter operated at 1–3 MHz; at 250 W, the inductor reduced converter losses by 19 %, compared to a conventional inductor design. In some cases, litz wire may further improve the performance of the proposed structure. With litz wire, the example inductor had an improved quality factor of 980. Thus, the proposed inductor geometry and design guidelines are suitable for small, highly efficient inductors at HF, and can thereby help realize high-frequency miniaturization of power electronics. (This paper is accompanied by an example Python script for generating preliminary designs, available online.)**

Keywords: inductors, magnetics, high frequency, distributed gap, skin effect

I. Introduction

Miniaturization of power electronics is often limited by the magnetic components due to high losses [2]. Although miniaturization of these components is still available with increased frequencies into the HF (3–30 MHz) range [3], significant design challenges remain. Skin and proximity effects play large roles at HF, where conventional litz wire solutions become less practical due to manufacturing difficulties for strands thinner than a skin depth [4]. Therefore, other approaches for reducing proximity effect, such as single-layer windings or multi-layer foil windings, have been investigated [4]–[7]. Fringing fields from gaps in the core also significantly increase winding loss, and various winding configurations and materials have been explored to deal with these effects [4], [8], [9]. In particular, distributed or quasi-distributed gaps have successfully mitigated fringing field effects [10] and are beginning to be implemented in cores on the market [11].

R. S. Yang, A. J. Hanson, and D. J. Perreault are with the Department of Electrical Engineering and Computer Science, Massachusetts Institute of Technology, Cambridge, MA 02139, USA (e-mail: rsyang@mit.edu; ajhanson@mit.edu; djperrea@mit.edu).

B. A. Reese and C. R. Sullivan are with the Thayer School of Engineering, Dartmouth College, Hanover, NH 03775, USA (e-mail: bradley.a.reese.th@dartmouth.edu; charles.r.sullivan@dartmouth.edu).

Part of this paper has been previously presented at the *2018 IEEE Applied Power Electronics Conference* in San Antonio, TX (March 4-8, 2018) [1].

To better understand the design challenges for magnetic components at HF, much research has focused on modeling. Analytical models of conductor loss [12]–[17] and core loss [18], [19] have been developed, with some work targeting the HF range [20]. While modeling can provide valuable analysis tools, development of HF structures and design guidelines is an additional important step.

We propose an inductor structure suitable for high-frequency operation with large ac currents (such that the magnetic field is constrained by loss and not saturation), along with analytic design guidelines to maximize its quality factor[1]. The proposed structure achieves high Q by using the available surfaces of the winding turns more effectively for conduction as a result of careful application of quasi-distributed gaps. Section II provides an overview of the proposed inductor geometry. The design guidelines are discussed in Section III, and automation of the design process is outlined in Section IV. In Section V, an example design is provided for a $16.6\,\mu$H inductor designed for 2 A (peak) of ac current at 3 MHz. The example achieves a quality factor of 700 in simulation, and simulation results verify that the design guidelines achieve the desired low-loss features. In Section VI, we present a hardware prototype that achieves an experimental Q of 720, agreeing with simulations. In addition, we demonstrate the prototype improving the efficiency and thermal performance of a high-frequency, high-current-swing power converter (1–3 MHz). In Section VII, we discuss using litz wire in the proposed structure to reduce loss, present additional design guidelines for litz, and demonstrate improved performance of the prototype inductor with litz wire ($Q = 980$). We conclude that the proposed structure can achieve high Q and that the analytic design guidelines are effective in designing high-Q inductors operating at high frequency with large ac current components.

II. Geometry Overview

The proposed core geometry resembles a pot core, but has a specific geometry with a single-layer winding and quasi-distributed gaps in the center post and outer shell (Fig. 1). To implement the quasi-distributed gaps, the core is composed of thin magnetically permeable discs and outer shell sections separated by small gaps. The center post and outer shell are bridged by magnetic end caps at the top and bottom of the

[1]This paper uses the following definition of quality factor: $Q = \omega L/ESR$.

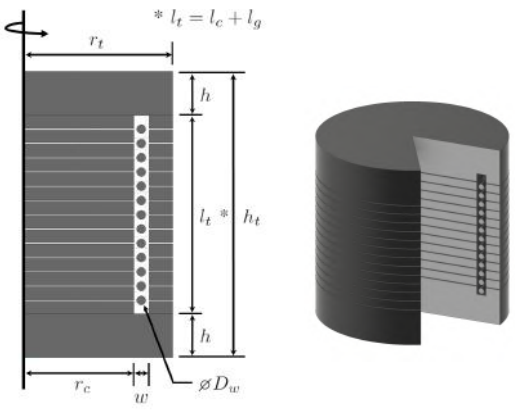

Fig. 1: Radial cross-sectional view (left) of the proposed inductor, with a center post, outer shell, and end caps encasing a single-layer winding. Parameters defining the geometry are labelled on this view as reference for Sections III and IV. Revolving the cross-section about the axis of rotation produces the 3D model of the inductor on the right (a piece is cut out for clarity).

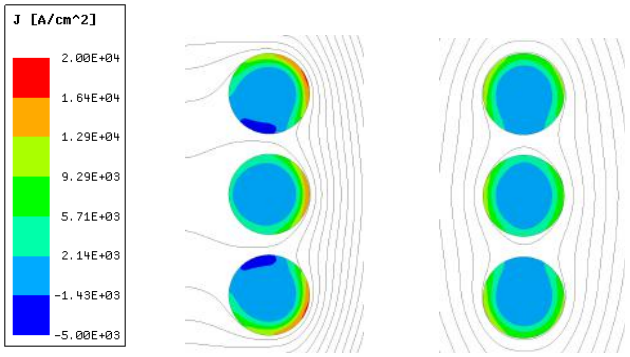

(a) Imbalanced H fields (b) Balanced H fields

Fig. 2: When H fields are balanced, the effective conduction area in the winding is increased. A winding with a lower H field on one side than the other side has only single-sided conduction (2a), while a winding with comparable H fields on either side has double-sided conduction (2b). The field imbalance/balance can be seen in the plotted B field lines.

structure. A single-layer winding is centered in the window, with evenly spaced turns.

This structure uses a single-layer winding to reduce proximity-effect losses and has a permeable return path to contain the flux, increase inductance, and improve the predictability of the inductance. The quasi-distributed gaps help reduce fringing field losses while still allowing the use of a high-permeability core material. Properly designed, the structure can also conduct current through a large fraction of the winding cross-sectional area, as explained in Section III-B.

III. Design Guidelines

The design guidelines below optimize the Q of the proposed structure at a given volume and inductance for applications where ac losses dominate. Most of the guidelines can be mathematically defined so that initial designs can be largely automated. A few of the parameters, however, must be manually tuned using the guidelines, as would be done in a non-analytic design process. Slight deviation from the optimized parameters, e.g. due to manufacturing tolerances, minimally impacts the Q of the structure, as the trade-off for each parameter falls off slowly near the optimum.[2]

A. Use quasi-distributed gaps to reduce gap fringing loss

Gapping ferrite cores in high-current-swing applications is important for keeping B fields low to reduce core loss, which scales as B^β ($\beta \approx$ 2–3), per the Steinmetz equation $P_v = k_c f^\alpha B^\beta$. As frequency increases, even lower B fields are needed to keep core loss low, leading to larger gaps. The impact of fringing fields from gaps on copper losses can thereby become more severe at higher frequencies. To reduce the fringing loss, the proposed inductor uses quasi-distributed gaps [10], as opposed to a conventional single lumped gap. Instead of dropping the entire MMF across one gap, the quasi-distributed gap has a smaller MMF across each of multiple gaps, causing less total loss in the winding. As shown in [10], the ratio of the pitch between the gaps (p) to the spacing between the gaps and the conductor (s) is an important parameter for fringing loss; [10] recommends $p < 4s$.[3] For the proposed structure, we set the number of gaps equal to the number of turns ($N_g = N$); Appendix A discusses how this selection, in tandem with the guidelines in Sections III-D and III-E, generally meets the $p < 4s$ criterion of [10].

B. Balance H fields to achieve multi-sided conduction

For a single-layer winding, copper loss at high frequencies is primarily due to skin effect, which reduces the effective area of current flow. In most cases, only a single side of the wire has a skin depth of conduction (not the entire circumference, as is commonly shown in textbooks for a wire in isolation). This single-sided conduction occurs in typical inductor geometries because the H fields near each turn are imbalanced, causing uneven current distribution (Fig. 2a). To reduce copper loss, the geometry should instead be designed to balance the H fields near each turn. If the H fields on either side of a turn are balanced, double-sided conduction can be achieved (Fig. 2b).

The proposed structure implements double-sided conduction to achieve low copper loss. To balance the H fields in this structure, the center post and the return path need to have equal reluctances (Fig. 3). Doing so makes the MMF drop ($\mathcal{F}$) across each region the same. Since both regions also have the same effective length (l), having equal $\mathcal{F}$ results in balanced H fields ($\mathcal{F} = Hl$).

To accurately design for equal reluctances, we include the overall fringing field outside the structure in the return path. Mathematically, we need

[2]The simulations in Section III show this minimal impact on Q near the optimum. This claim is also supported by a prototype inductor with manufacturing tolerances achieving high Q in accordance with its simulated Q (see Section VI).

[3]While increasing the number of gaps at lower pitch reduces fringing loss, it does so with diminishing returns and also makes construction increasingly difficult.

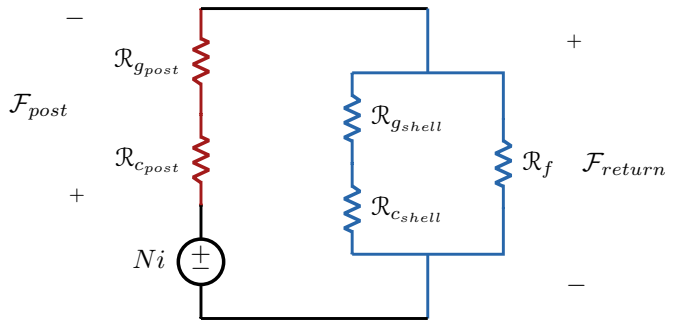

Fig. 3: Magnetic circuit model used to balance the H fields in the proposed structure by making the reluctances of the center post (red) and the return path (blue) equal. The discs of core material and the quasi-distributed gaps in the center post and the outer shell are treated as lumped reluctances. The end caps are composed of ungapped magnetic material and their reluctances are assumed to be negligible.

$$\mathcal{R}_{c_{post}} + \mathcal{R}_{g_{post}} = (\mathcal{R}_{c_{shell}} + \mathcal{R}_{g_{shell}}) \parallel \mathcal{R}_f \tag{1}$$

where $\mathcal{R}_{c_{post}}$ and $\mathcal{R}_{c_{shell}}$ are, respectively, the lumped reluctance of the discs of core material in the center post and in the outer shell, $\mathcal{R}_{g_{post}}$ and $\mathcal{R}_{g_{shell}}$ are, respectively, the lumped reluctance of the quasi-distributed gaps in the center post and in the outer shell, and $\mathcal{R}_f$ is the reluctance of the overall fringing path outside of the structure.

Neglecting local gap fringing, $\mathcal{R}_{c_{post}}$, $\mathcal{R}_{c_{shell}}$, $\mathcal{R}_{g_{post}}$, and $\mathcal{R}_{g_{shell}}$ can be calculated directly from the geometry (Fig. 1):

$$\mathcal{R}_{c_{post}} = \frac{l_c}{\mu_c \pi {r_c}^2} \quad (2) \qquad \mathcal{R}_{c_{shell}} = \frac{l_c}{\mu_c \pi ({r_t}^2 - (r_c + w)^2)} \quad (3)$$

$$\mathcal{R}_{g_{post}} = \frac{l_g}{\mu_0 \pi {r_c}^2} \quad (4) \qquad \mathcal{R}_{g_{shell}} = \frac{l_g}{\mu_0 \pi ({r_t}^2 - (r_c + w)^2)} \quad (5)$$

where l_c is the combined height of the core material discs, l_g is the overall length of the gap, and μ_c is the permeability of the core material.

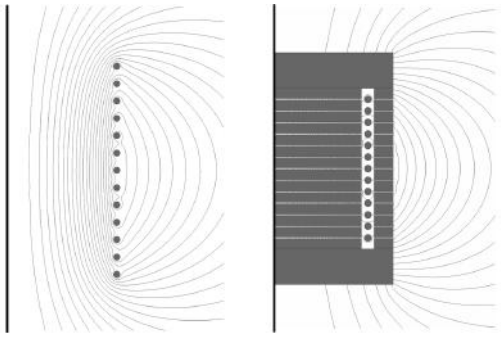

Fig. 4: A solenoid (left) and the proposed inductor (right) have similar fringing fields, so the fringing field reluctances can be modeled as approximately equal. This approximation is then used in calculations for balancing the H fields in the proposed inductor.

$\mathcal{R}_f$, however, is more difficult to calculate from first principles; instead, we estimate it using a solenoid model. Since the proposed inductor and a solenoid of the same size have similar overall fringing fields (Fig. 4), their fringing field reluctances are about the same. So, to estimate $\mathcal{R}_f$ of the proposed inductor, we can back out the fringing field reluctance from any appropriate solenoid inductance model. In general, for a solenoid,

$$L = \frac{N^2}{\mathcal{R}_{inside} + \mathcal{R}_f} \tag{6}$$

where $\mathcal{R}_{inside} = h_t/(\mu_0 \pi {r_t}^2)$ is the reluctance of the path through the center of the solenoid. By substituting a solenoid inductance model of our choosing into (6), we can then derive an expression for $\mathcal{R}_f$. For example, for structures where $h_t > \frac{2}{3} r_t$, the following air-core solenoid model [21] can be used:

$$L \approx \frac{\mu_0 N^2 \pi {r_t}^2}{h_t + 0.9 r_t} \tag{7}$$

We can then back out

$$\mathcal{R}_f \approx \frac{0.9}{\mu_0 \pi r_t} \tag{8}$$

For more general cases, the short solenoid model [22] may be more appropriate:

$$\widetilde{L} \approx 2 F N^2 \widetilde{r_t} \tag{9}$$

where $\widetilde{L}$ is the inductance in µH, $\widetilde{r_t}$ is the radius of the solenoid in inches, and F is an experimentally derived quantity defined in [22]. With this model,

$$\mathcal{R}_f \approx \frac{2.54 \times 10^4}{2 r_t F} - \frac{h_t}{\mu_0 \pi {r_t}^2} \tag{10}$$

Using $\mathcal{R}_f$, we can then design the center post and the return path to have equal reluctances, and thus balance the H fields to achieve double-sided conduction.

To validate this approach for estimating $\mathcal{R}_f$, inductors of the same volume ($14\,\mathrm{cm}^3$) but different aspect ratios were designed for the same inductance ($16.6\,\mu\mathrm{H}$) using (8). The inductors were then simulated, and the designed and simulated inductances had less than $10\,\%$ error across a wide range of aspect ratios (Table I).

TABLE I: Error of inductance model (Section III-B) for $16.6\,\mu\mathrm{H}$ designs

aspect ratio ($h_t/(2r_t)$)	simulated L (µH)	error (%)
2/3	17.4	4.6
1.0	18.0	8.5
2.0	17.0	2.4
3.0	16.2	2.7
4.0	16.7	0.3

C. Distribute B fields to reduce overall core loss

While H field balancing helps prevent circulating current losses in the winding, evenly distributed B fields in the core can reduce core loss. In the case of unevenly distributed B fields, regions with higher B fields experience much greater core loss, since core loss scales as B^{β}. The high core losses in these regions then result in greater total core loss.

Since $B = \mu H$, regions with the same permeability and H fields will have the same B fields. In the proposed inductor, the center post and the outer shell have the same effective permeability because they have the same overall gap and core lengths. Therefore, designing for balanced H fields in the proposed structure will also achieve evenly distributed B fields in these core regions. For cases in which the center post and the outer shell do not have the same effective permeability, the structure cannot achieve both balanced H fields and evenly distributed B fields. Instead, to minimize overall loss, the designer would need to find the optimal balance with partial double-sided conduction and a slight imbalance in the B field distribution.

For the end caps, the B field distribution, and thus core loss, is affected by their thickness. Thicker end caps allow the B field to distribute more in these regions for lower core loss, but with diminishing returns for added volume. The designer can use simulation to determine an end cap thickness that reduces loss without excessive volume.

D. Select a wire size that optimizes effective conduction area

Since the structure is designed to achieve double-sided conduction in the winding, larger diameter wire reduces copper loss by providing more circumferential conduction area. As the wire diameter increases, however, proximity effect losses between the turns play a larger role.

One metric for selecting a wire diameter (D_w) is the vertical window fill (F_v), defined as the fraction of the window height (l_t) that is occupied by conductive material, i.e.

$$F_v = \frac{N D_w}{h_t - 2h} \tag{11}$$

using the geometry in Fig. 1. Finite element analysis (FEA) simulations[4] show that a wire diameter yielding a vertical window fill between 50–80 % optimizes the total effective conduction area for these two competing effects (Fig. 5). For a given window height, the copper loss is largely insensitive to deviations in the wire diameter near the optimum.

E. Select a window size that balances gap fringing field loss and core loss in end caps to reduce overall loss

To minimize gap fringing field loss, the structure would ideally have a large window to increase the horizontal distance between the gaps and the winding. However, since flux crowding around the ends of the window leads to higher B fields in and near the end caps (Fig. 6), a larger window would increase core loss by increasing the volume of these high-B-field regions.

[4]All FEA simulations were run in ANSYS Maxwell, except for those in Section VII which were run in Finite Element Method Magnetics (FEMM).

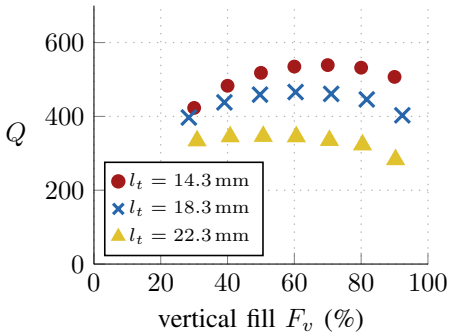

Fig. 5: For a given window height l_t, a wire diameter that yields a 50–80 % vertical window fill optimizes the total effective conduction area to reduce copper loss. To find this optimum, inductors with the same inductance (16.1 µH) and core geometry (r_t = 13.2 mm, h_t = 26.3 mm) but different conductor diameters were simulated. To make the gap fringing loss on the winding negligible, the inductors had a large window width that was 3 times the maximum wire diameter at F_v = 100%. As shown in the graph, the optimal range of vertical fill holds across different window heights.

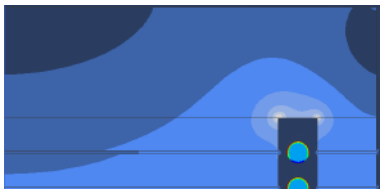

Fig. 6: Flux crowding at the end of the window leads to higher B fields (grey) and thus greater core loss.

One metric for selecting a window width (w) is the horizontal window fill (F_h), defined as the fraction of the window width that is occupied by conductive material, i.e.

$$F_h = \frac{D_w}{w} \tag{12}$$

using the geometry in Fig. 1. FEA simulations show that to balance the fringing loss and the end cap core loss, the horizontal window fill of the winding should be between 40–60 % (Fig. 7). So, for a given wire diameter D_w, the optimal window size is approximately $2D_w$, but the overall loss is largely insensitive to changes in the window size near the optimum.

F. Use a square aspect ratio to minimize overall loss

A "square" aspect ratio (diameter ≈ height) is the preferred overall geometry for this structure. FEA simulations of otherwise optimized inductors show that structures that are much wider than they are tall, or vice-versa, achieve lower Q (Fig. 8).

Conceptually, we can explain the disadvantages of unbalanced geometries by considering the end caps separately from the rest of the structure (everything within l_t). The section within l_t may be thought of as the "active" section where flux links the winding and substantial reluctance is provided,

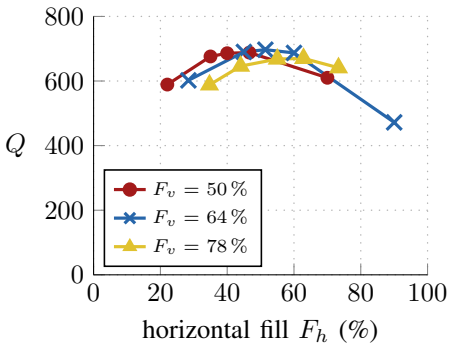

Fig. 7: For a given wire diameter, a window size with a 40–60 % horizontal fill for the winding balances the gap fringing loss and end cap core loss. To find this balance, inductors with the same inductance (16.5 µH) and volume ($r_t = 13.2\,\text{mm}$, $h_t = 26.3\,\text{mm}$) but different window widths were simulated. As shown in the graph, the optimal horizontal fill range holds across the optimal vertical fill (F_v) range.

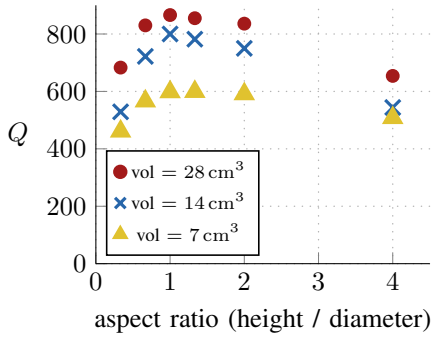

Fig. 8: Structures with a "square" aspect ratio achieve the optimum Q. To find this optimum, inductors with different aspect ratios but the same inductance (16.5 µH) and volume were simulated, and each design was optimized using the guidelines discussed in Sections III-A to III-G. As shown in the graph, the "square" aspect ratio is optimal across different volumes.

while the end caps may be thought of as overhead required to complete the magnetic path. These two sections have opposite loss dependencies on diameter: increasing diameter increases loss in the end caps by adding volume (for a fixed end cap height) but decreases loss in the active section[5]. This competing tendency explains why intermediate aspect ratios provide the best performance.

G. Approximately balance copper and core loss to reduce overall loss

In general, for a given core material, the number of turns and overall gap length in an inductor can be used to tune the copper and core losses. For inductors in which ac losses are dominant considerations over dc losses or saturation, the overall loss is usually minimized at a point where core loss is close to, but slightly less than copper loss [23]. To reduce the overall loss in the proposed structure, the designer can balance the copper and core losses accordingly by modeling the losses with exact core loss parameters or hand-tuning the design in simulation, as is done in conventional inductor designs.

IV. Automating Initial Designs of the Proposed Inductor Structure

Using the design guidelines discussed in Section III, we can mathematically define the proposed inductor geometry. The design process can then be largely automated to generate high-Q inductor designs for a desired volume and inductance at a given frequency and current (Fig. 9). The end cap height and the number of turns, however, must still be manually tuned. An example Python script for automating the design process can be found as a digital attachment to this paper online.

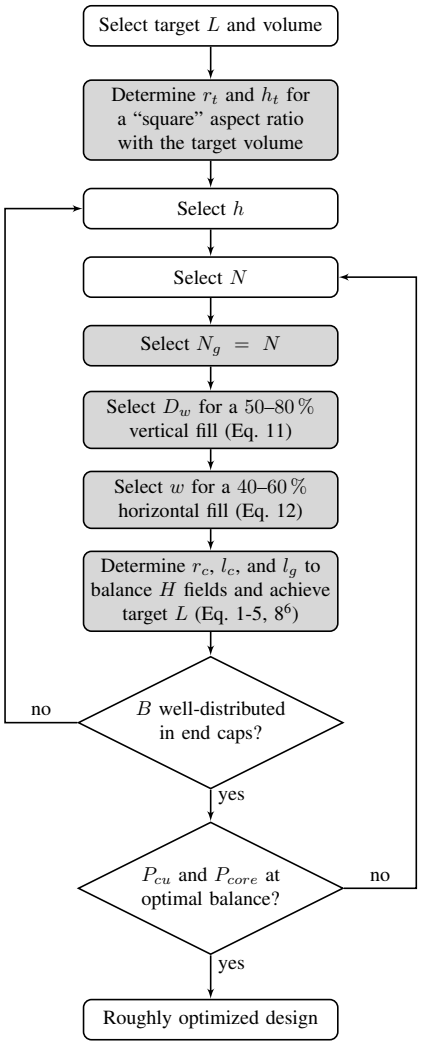

Fig. 9: Flowchart of the design process for the proposed inductor structure using the guidelines presented in Section III. The parameters used in the flowchart are labelled on the cross-sectional view in Fig. 1. Grey fill denotes steps that can be automated.

[5]For a first-order derivation showing that loss in the active section decreases as diameter increases, see Appendix B.

[6]Eq. 8 may be replaced with Eq. 10 or any other appropriate fringing field reluctance model.

V. An Example 16.6 µH Design: Simulations

Using the guidelines in Section III, we designed an example 16.6 µH inductor that achieved a Q of 700 at 3 MHz and 2 A (peak) of ac current in FEA simulation (Table II). To design the example inductor, a script was used. The target inductance and volume as well as a selected h and N were entered into the script, which generated dimensions for the geometry that were then simulated. Afterwards, the height of the end caps was manually tuned for well-distributed B fields, such that additional height would only slightly further distribute the fields and thus marginally reduce core loss in the end caps. The script was re-run with the optimized h. Next, designs with varying number of turns were generated using the script to find the optimum core and copper loss balance. At this point, the example design was roughly optimized. We then chose to continue with additional minor adjustments in FEA for further optimization (Table III).

TABLE II: Specifications for the simulated example inductor

Inductance	16.6 µH
Frequency	3 MHz
Current	2 A (peak, ac)
Core Material	Fair-Rite 67, $\mu_r = 40$ Steinmetz parameters: (P_v in mW/cm^3, f in MHz, $\hat{B}$ in mT) $k_c = 0.034$, $\alpha = 1.18$, $\beta = 2.24$

TABLE III: Geometry of the simulated example inductor (see Fig. 1)

Total Diameter ($2r_t$)	26.9 mm
Centerpost Radius (r_c)	9.9 mm
Window Width (w)	1.4 mm
Total Height (h_t)	26.0 mm
End Cap Height (h)	4.0 mm
Total Core Length (l_c)	16.5 mm
Total Gap Length (l_g)	1.5 mm
Number of Turns (N)	13
Number of Gaps (N_g)	13
Wire Diameter (D_w)	0.812 mm (20 AWG)

The simulation results verified that by following the design guidelines, the example design achieved all of the desired low-loss features, and thus a roughly optimized Q. The B fields in the center post and the shell were roughly equal for low core loss (Fig. 10a), and most turns had balanced H fields and associated double-sided conduction for low copper loss (Fig. 10b). It was verified that additional thickness to the end caps would have minimal effect on loss, and that larger or smaller window sizes would increase total loss. The core and copper loss were also verified to be well balanced.

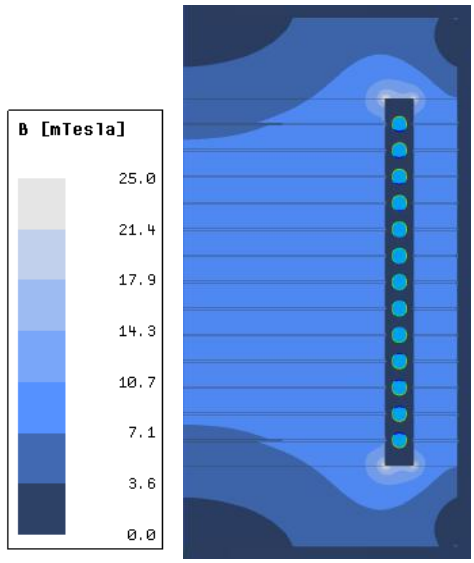

(a) Roughly even distribution of B fields

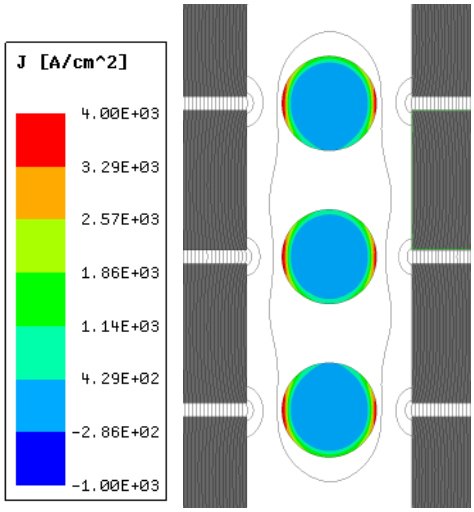

(b) Turns with double-sided conduction

Fig. 10: B field (blue), B field lines (black), and current distribution (rainbow) simulations of the example 16.6 µH inductor verifying that it achieves the desired low-loss features by following the design guidelines in Section III. These simulations are of the "worst-case" distributions for a helical winding, with each turn next to a gap. Other cross sections of the inductor would have turns in between the gaps and thus lower loss.

VI. An Example 16.6 µH Design: Experimental Results

We constructed a prototype (Fig. 11) of the example inductor presented in Section V.[7] The prototype inductor achieved a large-signal quality factor measurement[8] of $Q = 720$ at 3 MHz and 2 A (peak) of ac current (Table IV), which agrees with simulations. In addition, the prototype continued to have high Q outside of its optimized designed operating point. In

[7]For fabrication details of the prototype inductor, see Appendix C.
[8]For details on the large-signal Q measurement approach, see Appendix D.

this section, we demonstrate the performance of the inductor across drive level and at higher frequencies. We also show the prototype improving the efficiency and thermal performance of a high-current-swing power converter.

Fig. 11: Prototype inductor of the example design (Section V) having a measured Q of 720. Vertical windows in the outer shell were added to impede the circumferential component of flux and to allow the winding terminations to leave the structure.

TABLE IV: The simulated example inductor and the prototype with 20 AWG wire

	Simulated	Prototype
Inductance	16.6 µH	13.4 µH[9]
Q at 3 MHz, 2 A (peak, ac)	700	720

A. Experimental Q measurements of the prototype inductor verified simulations

The Q of the prototype inductor was measured across drive levels (0.5–3.5 A), and the experimental measurements closely matched the simulated quality factors (Fig. 12). This agreement experimentally verified the simulations, and the experimental Q measurements also verified that the guidelines in Section III achieve a high Q inductor.[10]

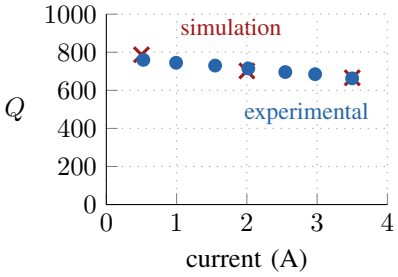

Fig. 12: The experimental Q measurements of the prototype inductor (Fig. 11) closely matched the simulated quality factors, thereby verifying the simulations and demonstrating that the guidelines in Section III can achieve a high Q inductor.

[9]The discrepancy between the simulated and prototype inductances can be partly attributed to permeability variations (a 25 % variation yields a 7 % error) and to the added vertical windows in the outer shell, which were not included in 2D simulation (yields a 2 % error).

[10]In some MnZn ferrite quasi-distributed designs, increased surface losses from multiple gaps have been observed [24]. For the prototype inductor, however, the agreement between the experimental and simulated quality factors indicates that any surface loss effects are minimal.

B. Prototype inductor achieves high Q at higher frequencies

The features that allow the prototype inductor to achieve high Q at 3 MHz, namely double-sided conduction and quasi-distributed gaps, continue to be beneficial at higher frequencies. In simulations at 4.5 MHz and 5.5 MHz[11], the example inductor achieved high quality factors ($Q \approx 700$) at 2 A (peak) of ac current (Fig. 13). The prototype inductor also had measured quality factors of $Q \approx 700$ at these two frequencies, demonstrating the structure's potential to achieve high Q at higher frequencies.

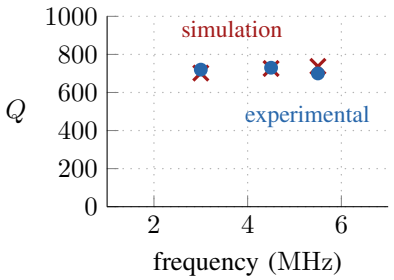

Fig. 13: The prototype inductor (Fig. 11) continued to have high quality factors at frequencies higher than its designed frequency of 3 MHz. Simulations and measurements were taken at 2 A (peak) of ac current.

C. Prototype inductor improved efficiency of a high-current-swing power converter

In addition to achieving a high Q under controlled conditions, the example inductor was used in a power factor correction converter operating at dynamically varying frequencies of 1–3 MHz and with large ac current components in the inductor [25]. The inductor improved converter performance significantly (Fig. 14) over a more conventional open-magnetic-circuit inductor (a half-toroid core approximating a rod core with litz wire) (Table V), despite having similar effective volume. This improvement can also be seen in thermal measurements: at a 93 W operating point, the conventional inductor saw a ∼30 °C temperature rise, while at a much higher power (296 W), the proposed inductor only saw a ∼3 °C rise (Fig. 15).

TABLE V: Specifications for the conventional inductor

Inductance	15 µH
Core Material	Fair-Rite 67, $\mu_r = 40$
Core Geometry	half-toroid (approximating a rod): $ID = 23$ mm, $OD = 35.55$ mm, $h = 12.7$ mm
Wire	5/9/10/48 litz (26 turns)

[11]For 4.5 MHz and 5.5 MHz, the Steinmetz parameters were $k_c = 0.00163$, $\alpha = 1.37$, and $\beta = 2.21$ (for P_v in mW/cm^3, f in MHz, $\hat{B}$ in mT). The parameters were derived using core loss data for Fair-Rite 67 from [3].

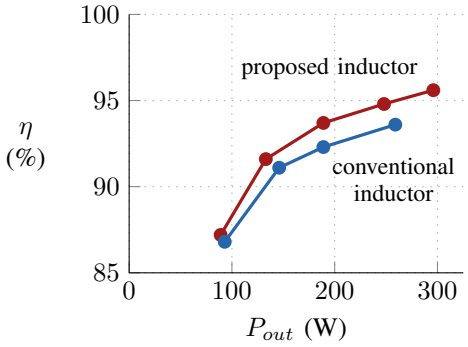

Fig. 14: The proposed inductor improved the efficiency of a power converter operating at 1–3 MHz at different output powers, compared to a conventional inductor.

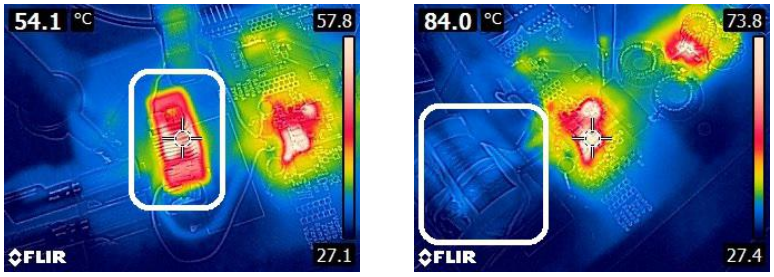

(a) conventional inductor ($\Delta T = \sim 30\,^{\circ}\mathrm{C}$ at $P_{out} = 93\,\mathrm{W}$)

(b) proposed inductor ($\Delta T = \sim 3\,^{\circ}\mathrm{C}$ at $P_{out} = 296\,\mathrm{W}$)

Fig. 15: Thermal images showing the proposed inductor (15b, white box) having a much smaller temperature rise for a higher converter output power than a more conventional open-magnetic-circuit inductor (15a, white box).

VII. Litz Wire in the Proposed Structure

While the example inductor in Section V can achieve low winding loss through double-sided conduction, a large fraction of the solid-core winding cross-sectional area still remains unused. In some cases, litz wire can have greater effective conduction area for improved performance in the proposed structure. For example, a litz wire version of the prototype inductor (Fig. 11) achieved a higher Q of 980 at the same frequency and drive level (3 MHz, 2 A (peak) of ac current). In this section, we describe design guidelines for optimizing litz wire and discuss the improved simulation and experimental results of the example inductor with litz wire.

A. Design guidelines for optimizing litz wire

As a starting point, the simple design procedure for economical litz wire presented in [26] can be used to optimize litz wire. For a given winding window, the procedure optimizes the number of strands and strand diameter for loss and cost. To estimate power loss, the ac resistance factor (F_R) is used and can be calculated by

$$F_R = \frac{R_{ac}}{R_{dc}} = 1 + \frac{(\pi n N_s)^2 d_s^6}{192 \cdot \delta^4 b^2} \tag{13}$$

where δ is the skin depth, b is the breadth of the winding window, N_s is the number of turns, n is the number of strands, and d_s is the strand diameter. When the strand diameter is close to or greater than the skin depth, however, (13) may not be accurate. Instead, the semi-empirical approach from [27] can be used to better estimate power loss.

The simple litz design procedure is useful, but it is agnostic to the construction of the litz wire, which can affect performance when d_s is not much less than δ, as may frequently be the case in high-frequency designs. Litz wire is constructed from strands of individually insulated wire that are twisted together into bundles; multiple bundles may be twisted together to form a larger effective wire, and such second-level bundles may also be twisted together to increase the effective wire size further. Thus, there are many ways to construct litz wire for a given number of strands and strand diameter. Since each level of bundling may experience skin and proximity effects similar to those experienced by solid core wire [28], the choice of construction can be important. To mitigate bundle-level skin effect, [26] recommends that the number of strands in the first twisting operation should be less than

$$n_{1,max} = 4\frac{\delta^2}{d_s^2} \tag{14}$$

Subsequent twisting operations should combine no more than five bundles. If for some reason these guidelines cannot be followed (e.g., using a standard litz wire design to reduce cost), bundle-level skin effect losses are no longer negligible and should be included when estimating power loss [27], [29].

In addition, when the strand diameter is close to or larger than the skin depth, the way the strands are twisted together can be important and should be included when estimating power loss. Bundles may be "bunched" together (indicated by the "/" symbol), meaning that the bundles are twisted in the same direction as the prior level bundles/strands. Alternatively, bundles may be "cabled" together (indicated by the "×" symbol), meaning that the bundles are twisted in the opposite direction. For example, the $5 \times 9 \times 10/48$ configuration in Fig. 16a is 10 strands of 48 AWG wire bunched together, then 9 of those bundles cabled together, and finally 5 of those bundles cabled together. The $5/9/10/48$ configuration in Fig. 16b has the same number of strands and bundles as $5 \times 9 \times 10/48$, but is bunched in each twisting operation rather than cabled. In this example, bunching achieves higher packing factor than cabling.

B. Simulations showed litz wire improving Q of prototype inductor at 3 MHz

Using the guidelines in Section VII-A, we investigated the effect of different litz wire designs on the performance of the example inductor (Section V) at 3 MHz. For these designs, we chose strands of 48 AWG since they are a good trade-off between cost and power loss at this frequency.[12]

[12]Power loss could be further reduced with finer strands; however, the costs of magnet wire manufacturing and litz construction increase rapidly for strands with wire gauge greater than 44 AWG.

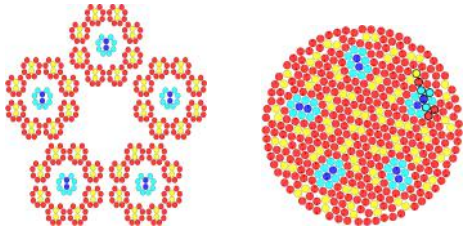

(a) $5 \times 9 \times 10/48$ (b) $5/9/10/48$

Fig. 16: Idealized cross-sections of litz wires with 450 strands using cabling (16a) and bunching (16b) twisting operations. The different colors of strands correspond to different circuit "shells" used to simulate bundle-level skin effect [27].

First, we used the simple litz wire design procedure [26] to estimate the optimal number of strands. Since the strand diameter is close to the skin depth at 3 MHz, we then used the semi-empirical approach from [27] to more accurately find an approximately optimal number of strands (275) and construction ($5 \times 5 \times 11/48$). We also used this approach to simulate a configuration that was readily available for experimental verification (450 strands, constructed as $5/9/10/48$) (Fig. 16b). Since the $5/9/10/48$ configuration is more susceptible to bundle-level skin effect, it was simulated with bundle-level skin effect (worst case) and without it (best case). Because of random perturbations in the positions of the strands in real litz wire, some bundle-level skin effect may be mitigated, and it is expected that experimental results will fall between the worst and best cases.

Simulation results show that litz wire can provide significant improvement over solid wire for the example inductor used throughout this paper (Fig. 17). The approximately optimal configuration ($5 \times 5 \times 11/48$) performs slightly better[13] than the simple litz model prediction by 7.9%, due to the self shielding effect that occurs when the strand diameter is close to the skin depth [27]. The readily available $5/9/10/48$ configuration under-performs the simple litz model by 6.6% when bundle-level skin effect is included.

C. Experimental Q measurements of litz wire prototype verified simulations

Using the same core geometry as the example inductor presented in Section V, we constructed a prototype inductor with the readily available $5/9/10/48$ litz wire. At 3 MHz and 2 A (peak) of ac current, the litz wire prototype achieved an experimental quality factor of $Q = 980$, agreeing with simulations (Table VI). For this operating point, litz wire provided a 36 % improvement in Q over solid-core wire. This improvement demonstrates the potential of litz wire to improve performance of the proposed structure for certain operating points.

[13]While the number of strands in the first twisting operation is higher than the recommendation from (14) ($n_{1,max} = 5$ at 3 MHz), it does not result in significant bundle-level skin effect in this case (a difference of 0.96% in Q).

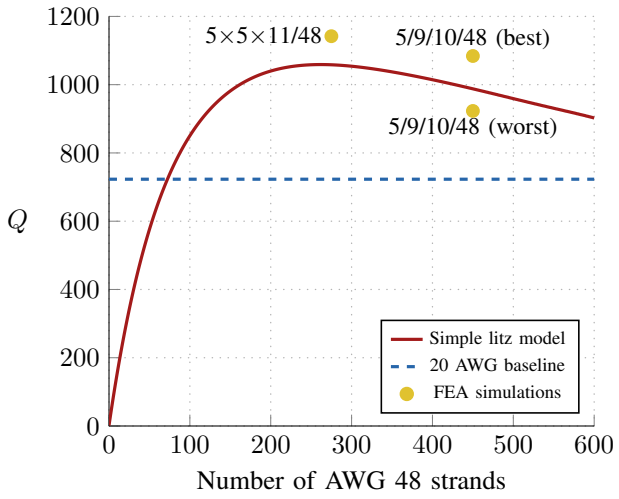

Fig. 17: Simulated inductor Q versus number of AWG 48 litz wire strands using a simple design method (red line) and FEA simulations of specific litz configurations (yellow points) at 3 MHz and 2 A (peak) of ac current. At this operating point, the example inductor can achieve higher Q with litz wire than with 20 AWG solid wire (blue dashed line).

TABLE VI: The simulated example inductor and the experimental prototype with $5/9/10/48$ litz wire

	Simulated (average case)	Prototype
Inductance	16.6 µH	12.6 µH
Q at 3 MHz, 2 A (peak, ac)	1000	980

D. Litz wire prototype can achieve high Q at high frequencies

At higher frequencies (up to 5.5 MHz), the litz wire prototype continued to achieve high Q at 2 A (peak) of ac current. However, since the litz wire in the prototype inductor was designed for 3 MHz, the performance using this particular construction ($5/9/10/48$) over 20 AWG wire declined at higher frequencies (Fig. 18). Other litz wire configurations optimized for higher frequencies, e.g. with fewer number of strands, could have lower high-frequency copper loss, and litz wire may still be beneficial at higher frequencies [27].

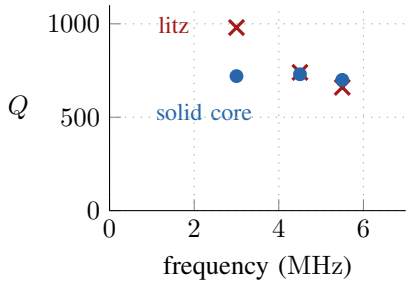

Fig. 18: Experimental results: Using $5/9/10/48$ litz wire instead of 20 AWG solid-core wire in the prototype inductor improved its Q at 3 MHz. This litz wire configuration, though, had worse performance above its optimized frequency of 3 MHz.

VIII. Conclusion

Design of highly efficient, miniaturized inductors in the HF range is a significant challenge. The proposed inductor structure and design approach provide a solution for low-loss high-frequency power inductors. Using a set of analytic design guidelines, designers can achieve a roughly optimized inductor for a desired inductance and volume and then choose to further refine the design in FEA using the general design rules. This geometry and its guidelines for achieving high Q were confirmed experimentally through an example inductor with a manufactured Q of 720. In some cases, using litz wire with this geometry can also improve its performance, and a Q of 980 was demonstrated with suitable litz wire.

Acknowledgment

This work was supported by the National Science Foundation under Grants 1609240 and 1610719, by Analog Devices through the MIT SuperUROP program, and by the Carl W. Hoffman (1980) and Elizabeth B. Klerman (1982) Fund. Support for this work was also provided by the Cooperative Agreement between the Masdar Institute of Science and Technology (Masdar Institute), Abu Dhabi, UAE and the Massachusetts Institute of Technology (MIT). We would also like to thank Fair-Rite for manufacturing the magnetic core pieces used in the prototypes.

Appendix A
Designing the Distributed Gap Geometry to Minimize Gap Fringing Loss

In this section, we show that setting the number of gaps N_g equal to the number of turns N aligns closely with the recommendation for minimizing gap fringing loss from [10], where the pitch between gaps (p) should be less than four times the spacing between the gap and the conductor (s), or $p < 4s$. We assume a large N so that the center-to-center spacing between each turn (p_w) can be approximated as $p_w = l_t/(N+1) \approx l_t/N$, where l_t is the window height. Setting $N_g = N$ also sets $p = p_w$, so the vertical and horizontal window fill are then

$$F_v = \frac{ND_w}{l_t} \approx \frac{D_w}{p} \quad (15) \qquad F_h = \frac{D_w}{w} \quad (16)$$

where D_w is the wire diameter and w is the window width (Fig. 1) Based on the geometry, the spacing between the gap and the winding is

$$s = \frac{w - D_w}{2} \quad (17)$$

By combining (15)−(17), we get

$$\frac{p}{s} = \frac{2F_h}{F_v(1-F_h)} \quad (18)$$

Most combinations of F_v and F_h within the recommended ranges (Sections III-D and III-E) satisfy the design criteria from [10], $p < 4s$. For example, for values in the center of these ranges, $F_v = 0.65$ and $F_h = 0.50$, $p/s = 3.1 < 4$. At the edge of these ranges where F_v is small and F_h is large, the p/s ratio surpasses the recommendation of $p/s < 4$, with the worst case at $p/s = 6$, when $F_v = 0.50$ and $F_h = 0.60$. These edge cases, however, still achieve roughly optimal designs. Therefore, setting $N_g = N$ yields designs for the proposed inductor that meet (or nearly meet) the design criterion of [10] and thus, achieve roughly optimum Q.

Appendix B
First-Order Derivation of Loss in the Active Section

In this section, we quantitatively show to first-order that the loss of the active section of the structure (everything within l_t) decreases as the diameter increases. To do this, we consider the equivalent resistance of the active section.

The winding resistance is

$$R_w = \rho N \frac{2\pi r_c}{A_1} = \rho k_w N^2 \frac{2\pi r_c}{l_t} \quad (19)$$

where it is assumed that the available conduction area of a turn A_1 is proportional to the area of the window with the proportionality constant $1/k_w$, i.e. $A_1 = l_t/(k_w N)$, and the radius of the winding path is approximated as the center post radius r_c.

For the equivalent resistance of the core loss in the active section, we consider only the center post core loss for simplicity, since the outer shell core loss is on the same order. The core loss in the center post is given by

$$\begin{aligned} P_{core} = k_c(l_t \pi {r_c}^2) \times \hat{B}^\beta &= k_c(l_t \pi {r_c}^2) \times \left(\frac{LI_{pk}}{N\pi {r_c}^2}\right)^\beta \\ &\approx k_c(l_t \pi {r_c}^2) \times \left(\frac{LI_{pk}}{N\pi {r_c}^2}\right)^2 \end{aligned} \quad (20)$$

where we approximate $\beta = 2$ (not uncommon for low frequencies; usually an under-estimate at high frequencies). We may then express core loss through an equivalent resistance,

$$R_{core} = P_{core}/I_{rms}^2 = 2k_c l_t \frac{L^2}{N^2 \pi {r_c}^2} \quad (21)$$

In an optimized design, core loss is approximately equal to winding loss. Equating the resistances yields

$$N_{opt} = \left(\frac{k_c l_t^2 L^2}{\rho k_w \pi^2 {r_c}^3}\right)^{1/4} \quad (22)$$

$$R_w = R_{core} = \rho k_w {N_{opt}}^2 \frac{2\pi r_c}{l_t} = 2L\sqrt{\frac{\rho k_w k_c}{r_c}} \propto \sqrt{\frac{1}{r_c}} \quad (23)$$

so that the total equivalent resistance of the active section is proportional to $\sqrt{1/r_c}$. Thus, the loss in this section decreases as diameter increases.

Appendix C
Prototype Construction

Below, we provide fabrication details of the prototype inductor from Section VI-A for those interested in prototyping

processes. The construction method below is not intended as a viable mass production process.

The prototype inductor was constructed modularly with the aid of custom 3D-printed fixtures. The center post was constructed first (Fig. 19a) with one of the end caps. To control the quasi-distributed gaps, we stacked laser cut pieces of polyester plastic shimstock with the appropriate thickness ($0.114\,\mathrm{mm}$) in between each layer of core material. To center all of the center post layers, a $1\,\mathrm{mm}$ diameter hole was drilled in the center of the discs and the center post shimstock pieces so they could be assembled on a rod. Since the drilled holes were relatively small, we expect minimal effect on the fields.

For the winding, 20 AWG solid core wire with Teflon fluorinated ethylene propylene (FEP) insulation was wound around a 3D-printed fixture of the same diameter as the center post (Fig. 19b). The wire was chosen to have the appropriate insulation thickness ($0.229\,\mathrm{mm}$ from the conductor diameter to the outer diameter) to center it in the window. Then, the winding was wrapped in a single layer of $0.079\,\mathrm{mm}$ thick polypropylene tape (package sealing tape) to maintain its shape, removed from the fixture and put on the center post.

The outer shell, composed of three sections to allow for vertical windows (with approximate widths of $1.5\,\mathrm{mm}$), was constructed one section at a time. Each section was stacked on a 3D-printed fixture, alternating between layers of core material and laser cut shimstock (Fig. 19c). The outer surface of each section was taped to hold all the pieces together. Then, the sections were added to the center post structure so that the two winding terminations could leave the structure through one of the vertical windows in the shell.

Afterwards, the second end cap was added, and the rod was removed from the centerpost. Finally, the entire circumference of the inductor was wrapped with a single layer of package sealing tape to apply radial pressure, and a strip of package sealing tape was wrapped vertically around the inductor to apply vertical pressure.

(a) Center post (b) Winding (c) Outer shell section

Fig. 19: Construction of the prototype inductor using custom 3D-printed fixtures (white).

APPENDIX D
MEASURING HIGH Q (LARGE-SIGNAL)

To measure the large-signal Q of the prototype inductors, we used the same resonant measurement approach from [3] and [30] and added some modifications for measuring high Q. The original approach operates a series LC circuit at resonance so that the ratio of the peak capacitor voltage to the peak input voltage can be approximated as the Q of the inductor. When measuring a high Q, though, several assumptions in this approach no longer hold, leading to two modifications. Below, we discuss these modifications and other considerations for high-Q measurements at high frequency. We also show the validation of this modified measurement approach with an air-core inductor.

A. Use a capacitor divider to minimize probe loss and loading

When measuring a high-Q inductor, we expect a high resonant capacitor voltage. The probe loss and loading at this high-frequency, high-voltage node, however, can significantly affect results. To get a more accurate measurement of the resonant capacitor voltage, we replaced the capacitor in the original approach with a capacitor divider having the same net impedance. The stepped-down voltage can then be measured with minimal probe loss and loading (Fig. 20).

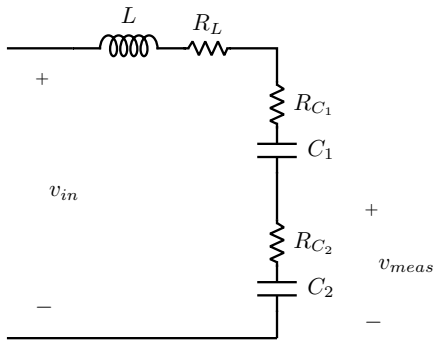

Fig. 20: Circuit for the resonant measurement approach to measure high Q, modified to include a capacitor divider to step down the measured output voltage. The capacitor ESRs are also included.

B. Include capacitor ESR to accurately measure high Q

For measuring high Q, the approximation made in [3] and [30] that the equivalent series resistances (ESRs) of the capacitors (R_{C_1}, R_{C_2}) are small compared to the equivalent series resistance of the inductor (R_L) no longer holds, even with NP0, porcelain, or mica capacitors. For example, to measure an inductor with $Q = 1000$, using mica capacitors with $Q = 4000$ would still introduce a 25% loss error in the measurement.

Since the capacitor ESRs are no longer negligible, we include them in deriving an expression for the quality factor of the inductor (Q_L), using the measured input voltage v_{in} and stepped-down voltage v_{meas}. From Fig. 20, we can see that at resonance, since the impedances of the inductor and capacitors cancel,

$$\frac{V_{meas,pk}}{V_{in,pk}} = \left| \frac{R_{C_2} + \frac{1}{j\omega_0 C_2}}{R_{C_1} + R_{C_2} + R_L} \right| \tag{24}$$

We also know that at resonance,

$$Q_L = \frac{\omega_0 L}{R_L} \tag{25}$$

From (24) and (25), the quality factor of the inductor as a function of $V_{in,pk}$ and $V_{meas,pk}$ is

$$Q_L = \frac{\omega_0 L}{\frac{V_{in,pk}}{V_{meas,pk}} \sqrt{{R_{C_2}}^2 + (\frac{1}{\omega_0 C_2})^2} - R_{C_1} - R_{C_2}} \tag{26}$$

where R_{C_1} and R_{C_2} are the ESR values found on the datasheet for the capacitors.[14]

The non-negligible capacitor ESR loss was validated thermally. At around 3 MHz, the highlighted mica capacitor in Fig. 21 has an ESR of $\sim 0.07\,\Omega$, as extrapolated from the datasheet. With 2.0 A of current and a thermal resistance of $95\,^\circ\mathrm{C/W}$ for the closest standard package size (2010) [31], we expect the capacitor to have a $\sim 13\,^\circ\mathrm{C}$ temperature rise, which agrees with the thermal image. This agreement confirms that the capacitor ESR loss can be predicted, and thus, corrected for when measuring the Q of the inductor.

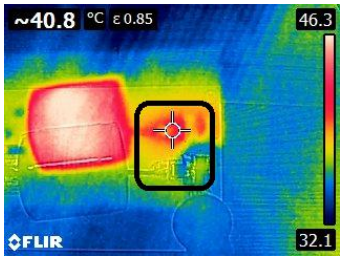

Fig. 21: Thermal image showing a mica capacitor (black box) with a $\sim 13\,^\circ\mathrm{C}$ temperature rise due to its ESR loss, in accordance with calculations.

C. Minimize dielectric loss through careful board layout

For measuring a high-Q inductor, the node between the inductor and the capacitor divider sees a high voltage at HF. Therefore, in a layout where the return path runs directly under this high voltage node, the resulting parasitic capacitor can have non-negligible dielectric loss. We can mathematically show this by modeling the dielectric loss as the ESR loss of the parasitic capacitor. The dielectric loss is

$$P_{loss} = \frac{1}{2} V^2 \omega C \tan\delta \tag{27}$$

where V is the peak voltage at the node, ω is the measurement frequency, C is the parasitic capacitance, and $\tan\delta$ is the dielectric loss tangent of the board material.

As seen from (27), nodes with high voltages ($\sim 1000\,\mathrm{V}$) can have substantial dielectric loss, especially when their parasitic capacitance and the dielectric loss tangent of the board are relatively large. For example, for measuring the Q of the example inductor (Fig. 11), the high voltage node expects $\sim 600\,\mathrm{V}$ at 3 MHz. If the node has an area of $1\,\mathrm{cm}^2$ on a standard 1.6 mm-thick FR-4 board ($\tan\delta = 0.02$), the dielectric loss at this node is then 160 mW, which is about 20 % of the inductor loss.

To minimize the dielectric loss, the capacitance at the high voltage node should be minimized by using a small node area and thick board. Board material with a lower dielectric loss tangent than FR-4, e.g. Rogers 4350B, can also be considered.

D. Resonant measurement approach validated using an air-core inductor

We validated the large-signal measurement approach described above with small-signal Q measurements of an air-core inductor. Since an air-core inductor has no nonlinear core loss, its small-signal and large-signal quality factors are the same. Using the equivalent series resistance of an air-core inductor measured at 3 MHz (with an Agilent 4395A Impedance Analyzer and a custom resonant fixture), the small-signal quality factor of the inductor was calculated to be $Q = 540$ at this frequency. Using the large-signal resonant measurement approach, the same air-core inductor had a measured quality factor of $Q = 500$ at 3 MHz and 2 A (peak) of ac current, which validates this approach for measuring large-signal Q in this range. For even higher Q (>1000), sources of error have a greater impact on measurements, which makes it more difficult to accurately measure Q. The validation of the air-core inductor at $Q = 500$, however, indicates that it is possible to accurately measure even higher Q using this measurement approach.

[14] In cases where the capacitors are physically composed of multiple capacitors in parallel, the ESRs R_{C_1} and R_{C_2} can each be approximated as the equivalent parallel resistance for the corresponding ESRs. C_1 and C_2 can also be approximated as the equivalent parallel capacitance of the capacitors comprising it.

References

[1] R. S. Yang, A. J. Hanson, D. J. Perreault, and C. R. Sullivan, "A low-loss inductor structure and design guidelines for high-frequency applications," in *2018 IEEE Applied Power Electronics Conference and Exposition (APEC)*, March 2018, pp. 579–586.

[2] C. R. Sullivan, B. A. Reese, A. L. F. Stein, and P. A. Kyaw, "On size and magnetics: Why small efficient power inductors are rare," in *2016 International Symposium on 3D Power Electronics Integration and Manufacturing (3D-PEIM)*, June 2016, pp. 1–23.

[3] A. J. Hanson, J. A. Belk, S. Lim, C. R. Sullivan, and D. J. Perreault, "Measurements and performance factor comparisons of magnetic materials at high frequency," *IEEE Transactions on Power Electronics*, vol. 31, no. 11, pp. 7909–7925, Nov 2016.

[4] C. R. Sullivan, "Prospects for advances in power magnetics," in *CIPS 2016; 9th International Conference on Integrated Power Electronics Systems*, March 2016, pp. 1–9.

[5] P. A. Kyaw, A. L. F. Stein, and C. R. Sullivan, "High-q resonator with integrated capacitance for resonant power conversion," in *2017 IEEE Applied Power Electronics Conference and Exposition (APEC)*, March 2017, pp. 2519–2526.

[6] A. L. F. Stein, P. A. Kyaw, and C. R. Sullivan, "High-q self-resonant structure for wireless power transfer," in *2017 IEEE Applied Power Electronics Conference and Exposition (APEC)*, March 2017, pp. 3723–3729.

[7] C. R. Sullivan, "Aluminum windings and other strategies for high-frequency magnetics design in an era of high copper and energy costs," in *APEC 07 - Twenty-Second Annual IEEE Applied Power Electronics Conference and Exposition*, Feb 2007, pp. 78–84.

[8] J. Qiu, A. Hanson, and C. Sullivan, "Design of toroidal inductors with multiple parallel foil windings," in *14th Workshop on Control and Modeling for Power Electronics (COMPEL)*. IEEE, 2013, pp. 23–26.

[9] Y. Han and D. J. Perreault, "Inductor design methods with low-permeability rf core materials," *IEEE Transactions on Industry Applications*, vol. 48, no. 5, pp. 1616–1627, Sept 2012.

[10] J. Hu and C. R. Sullivan, "The quasi-distributed gap technique for planar inductors: design guidelines," in *IAS '97. Conference Record of the 1997 IEEE Industry Applications Conference Thirty-Second IAS Annual Meeting*, vol. 2, Oct 1997, pp. 1147–1152.

[11] "Distributed air gaps in ferrite cores," EPCOS AG – a TDK Group Company, Tech. Rep., June 2017. [Online]. Available: https://de.tdk.eu/download/2113422/321697054fce0c768ea66959fde3b3db/ferrites-air-gaps-pb.pdf

[12] P. L. Dowell, "Effects of eddy currents in transformer windings," *Electrical Engineers, Proceedings of the Institution of*, vol. 113, no. 8, pp. 1387–1394, August 1966.

[13] C. R. Sullivan, "Optimal choice for number of strands in a litz-wire transformer winding," *IEEE Transactions on Power Electronics*, vol. 14, no. 2, pp. 283–291, Mar 1999.

[14] W. G. Hurley, E. Gath, and J. G. Breslin, "Optimizing the ac resistance of multilayer transformer windings with arbitrary current waveforms," *IEEE Transactions on Power Electronics*, vol. 15, no. 2, pp. 369–376, Mar 2000.

[15] T. Delaforge, H. Chazal, J. L. Schanen, and R. J. Pasterczyk, "Increasing windings efficiency at high frequencies: Hollow conductors and clad metal conductors formal solution based on the magnetic potential," in *2015 IEEE Energy Conversion Congress and Exposition (ECCE)*, Sept 2015, pp. 5689–5695.

[16] X. Nan and C. R. Sullivan, "An improved calculation of proximity-effect loss in high-frequency windings of round conductors," in *Power Electronics Specialist Conference, 2003. PESC '03. 2003 IEEE 34th Annual*, vol. 2, June 2003, pp. 853–860 vol.2.

[17] M. Chen, M. Araghchini, K. K. Afridi, J. H. Lang, C. R. Sullivan, and D. J. Perreault, "A systematic approach to modeling impedances and current distribution in planar magnetics," *IEEE Transactions on Power Electronics*, vol. 31, no. 1, pp. 560–580, Jan 2016.

[18] K. Venkatachalam, C. R. Sullivan, T. Abdallah, and H. Tacca, "Accurate prediction of ferrite core loss with nonsinusoidal waveforms using only steinmetz parameters," in *2002 IEEE Workshop on Computers in Power Electronics, 2002. Proceedings.*, June 2002, pp. 36–41.

[19] J. Muhlethaler, J. Biela, J. W. Kolar, and A. Ecklebe, "Improved core-loss calculation for magnetic components employed in power electronic systems," *IEEE Transactions on Power Electronics*, vol. 27, no. 2, pp. 964–973, Feb 2012.

[20] C. Fei, F. C. Lee, and Q. Li, "High-efficiency high-power-density llc converter with an integrated planar matrix transformer for high output current applications," *IEEE Transactions on Industrial Electronics*, vol. PP, no. 99, pp. 2428–2435, 2017.

[21] T. H. Lee, *Planar Microwave Engineering: A Practical Guide to Theory, Measurement, and Circuits*, 1st ed. Cambridge University Press, 2004, pp. 140–142.

[22] F. E. Terman, *Radio Engineers' Handbook*, 1st ed. McGraw-Hill Book Company, Inc., 1943, pp. 52–55.

[23] V. Valchev and A. Van den Bossche, *Inductors and Transformers for Power Electronics*. CRC Press, 2005.

[24] J. W. Kolar, F. Krismer, M. Leibl, D. Neumayr, L. Schrittwieser, and D. Bortis, Impact of Magnetics on Power Electronics Converter Performance – State-of-the-Art and Future Prospects, Keynote Presentation at the PSMA Workshop on "Power Magnetics @ High Frequency – Transforming the Black Magic to Engineering", Tampa, FL, USA, March 25, 2017.

[25] A. J. Hanson and D. J. Perreault, "A high frequency power factor correction converter with soft switching," in *IEEE Applied Power Electronics Conference (APEC)*, 2018.

[26] C. R. Sullivan and R. Y. Zhang, "Simplified design method for litz wire," in *IEEE App. Pow. Electr. Conf. (APEC)*, 2014, pp. 2667–2674.

[27] B. A. Reese, R. Joseph, and C. R. Sullivan, "Improved litz wire designs for the MHz range," in *2018 IEEE 19th Workshop on Control and Modeling for Power Electronics (COMPEL)*, June 2018.

[28] J. D. Pollock, T. Abdallah, and C. R. Sullivan, "Easy-to-use CAD tools for litz-wire winding optimization," in *IEEE App. Pow. Electr. Conf.*, 2003.

[29] C. R. Sullivan and R. Y. Zhang, "Analytical model for effects of twisting on litz-wire losses," in *IEEE Workshop on Control and Modeling for Pow. Electr. (COMPEL)*, 2014.

[30] Y. Han, G. Cheung, A. Li, C. Sullivan, and D. Perreault, "Evaluation of magnetic materials for very high frequency applications," *IEEE Transactions on Power Electronics*, pp. 425–435, 2008.

[31] "Power dissipation in high precision vishay sfernice chip resistors and arrays (p thin film, pra arrays, chp thick film)," Vishay, Tech. Rep., June 2018. [Online]. Available: https://www.vishay.com/docs/53048/pprachp.pdf

Rachel S. Yang (S'18) received the B.S. degree in electrical engineering from the Massachusetts Institute of Technology, Cambridge, MA in 2018. She is currently working toward the M.Eng. degree at MIT.

Alex J. Hanson (S'15) received the B.E. degree in electrical engineering (with highest hons.) from the Thayer School of Engineering at Dartmouth College, Hanover, NH, USA, in 2014, and the S.M degree from the Massachusetts Institute of Technology, Cambridge, MA, USA, in 2016, where he is currently working toward the Ph.D. degree.

His research interests include component- and system-level power electronics with emphasis on high-frequency magnetics and circuits.

Mr. Hanson received the William Portnoy 1st prize award from the IAS-PEDCC in 2016.

Bradley A. Reese (M'03) received the B.S. and M.S. degrees in electrical engineering from the University of Arkansas, Fayetteville, AR, USA, in 2006 and 2012, respectively. He is currently pursuing the Ph.D. degree with Dartmouth College, Hanover, NH, USA.

Before joining Dartmouth, he was with Arkansas Power Electronics, Fayetteville, AR, USA, where he focused on circuit design for extreme environment power electronics systems. His current research interests include high-frequency magnetic component design and new magnetic materials.

Charles R. Sullivan (S93-M96-SM12-F14) received the B.S. (Hons.) degree in electrical engineering from Princeton University, Princeton, NJ, USA, in 1987, and the Ph.D. degree in electrical engineering from the University of California, Berkeley, CA, USA, in 1996. Between the B.S. and Ph.D. degrees, he was with Lutron Electronics designing electronic ballasts.

He is currently a Professor at Thayer School of Engineering at Dartmouth, Hanover, NH, USA. His research interests include modeling and design optimization of magnetics and other passive components for high-frequency power conversion and wireless power transfer.

Dr. Sullivan received the Power Electronics Society Modeling and Control Technical Achievement Award in 2018 and has received three Power Electronic Society Prize Paper Awards.

David J. Perreault (S'91-M'97-SM'06-F'13) received the B.S. degree from Boston University, Boston, MA, and the S.M. and Ph.D. degrees from the Massachusetts Institute of Technology, Cambridge, MA.

In 1997 he joined the MIT Laboratory for Electromagnetic and Electronic Systems as a Postdoctoral Associate, and became a Research Scientist in the laboratory in 1999. In 2001, he joined the MIT Department of Electrical Engineering and Computer Science, where he is presently Professor of Electrical Engineering. He has held multiple roles within the EECS department, most recently as Associate Department Head from November 2013 to December 2016. His research interests include design, manufacturing, and control techniques for power electronic systems and components, and in their use in a wide range of applications. He also consults in industry, and co-founded Eta Devices, inc. (acquired by Nokia in 2016) and Eta Wireless, inc., startup companies focusing on high-efficiency RF power amplifiers.

Dr. Perreault received the Richard M. Bass Outstanding Young Power Electronics Engineer Award, the R. David Middlebrook Achievement Award, the ONR Young Investigator Award, and the SAE Ralph R. Teetor Educational Award, and is co-author of eleven IEEE prize papers.